

# Thalamic projections sustain prefrontal activity during working memory maintenance

Scott S Bolkan<sup>1</sup>, Joseph M Stujenske<sup>1</sup>, Sebastien Parnaudeau<sup>2</sup>, Timothy J Spellman<sup>3</sup>, Caroline Rauffenbart<sup>4,5,7</sup>, Atheer I Abbas<sup>4,6</sup>, Alexander Z Harris<sup>4,6</sup>, Joshua A Gordon<sup>4,6,8</sup> & Christoph Kellendonk<sup>4,5,7</sup>

The mediodorsal thalamus (MD) shares reciprocal connectivity with the prefrontal cortex (PFC), and decreased MD–PFC connectivity is observed in schizophrenia patients. Patients also display cognitive deficits including impairments in working memory, but a mechanistic link between thalamo–prefrontal circuit function and working memory is missing. Using pathway-specific inhibition, we found directional interactions between mouse MD and medial PFC (mPFC), with MD-to-mPFC supporting working memory maintenance and mPFC-to-MD supporting subsequent choice. We further identify mPFC neurons that display elevated spiking during the delay, a feature that was absent on error trials and required MD inputs for sustained maintenance. Strikingly, delay-tuned neurons had minimal overlap with spatially tuned neurons, and each mPFC population exhibited mutually exclusive dependence on MD and hippocampal inputs. These findings indicate a role for MD in sustaining prefrontal activity during working memory maintenance. Consistent with this idea, we found that enhancing MD excitability was sufficient to enhance task performance.

The PFC is a locus for higher-order cognition and executive control across species<sup>1</sup>. In several mental disorders including schizophrenia, PFC dysfunction is observed in concert with a variety of cognitive impairments, including deficits in working memory<sup>2–4</sup>. However, there is growing appreciation that PFC function cannot be divorced from that of its densely interconnected thalamic partners, such as the MD<sup>5–7</sup>. Indeed, not only does the PFC share dense reciprocal connectivity with the MD<sup>8</sup>, manipulations of MD function in animals produce cognitive impairments reminiscent of PFC dysfunction<sup>9–12</sup>. Brain imaging studies have also shown MD dysfunction in patients with schizophrenia<sup>13,14</sup>, with increasing evidence for decreased functional connectivity between the thalamus and PFC<sup>15–17</sup>. In spite of these findings, a circuit-level understanding of how thalamo–prefrontal circuits engage in cognition is lacking. Such an understanding will be essential to elucidating how circuit alterations contribute to cognitive dysfunction in disorders such as schizophrenia.

To address this issue, we investigated thalamo–prefrontal interactions during a spatial working memory task, in which mice had to choose a spatial location that differed from one they had sampled before a brief delay. Notably, spatial location varied on a pseudorandom trial-by-trial basis, thus requiring mice to maintain only information relevant to the present trial. Using both pathway-specific optogenetic inhibition experiments and directionality analyses of multisite recordings, we found that different task phases (sample, delay and choice) exhibited distinct thalamo–prefrontal dependencies. While initial spatial sampling required no functional interactions between MD and mPFC, spatial choice required

a directional interaction from mPFC to MD. In comparison, the delay phase required reciprocal interactions across the two structures, with inputs from MD to mPFC exerting a stronger influence on behavior. Notably, and despite this clear behavioral dependence, mPFC neurons showed no evidence for maintaining a spatial memory across the delay, although mPFC spatial coding was readily detected during both the sample and choice phases. However, a subset of mPFC neurons demonstrated elevated delay-phase spiking that indicated correct performance and was highly dependent on functional MD inputs. In a direct comparison of spatially tuned and delay-elevated mPFC neurons, we observed a double dissociation in their activity dependence on ventral hippocampal (vHPC) and MD inputs. Moreover, this effect was specific to the task phase in which each population was feature-selective, suggesting a circuit-specific role for MD inputs in sustaining prefrontal activity across working memory delays. Consistent with this idea, we found that temporally restricted enhancement of MD excitability during the delay was sufficient to improve working memory performance.

Combined, these findings demonstrate a functional dissociation of prefrontal substrates for spatial encoding, maintenance and retrieval of working memory. We conclude that, while vHPC inputs to the mPFC support spatial encoding, as previously shown<sup>18</sup>, MD inputs to the mPFC support the maintenance of working memory by stabilizing task-relevant prefrontal activity during the delay period and top-down signals from the mPFC back to the MD guide successful memory retrieval and/or action execution.

<sup>1</sup>Graduate Program in Neurobiology and Behavior, Columbia University, College of Physicians and Surgeons, New York, New York, USA. <sup>2</sup>Sorbonne Universités, UPMC Paris 06, Institut de Biologie Paris Seine, UM119, Neuroscience Paris Seine, CNRS UMR8246, INSERM U1130, Paris, France. <sup>3</sup>Feil Family Brain and Mind Research Institute, Weill Cornell Medical College, New York, New York, USA. <sup>4</sup>Department of Psychiatry, Columbia University, College of Physicians and Surgeons, New York, New York, USA. <sup>5</sup>Department of Pharmacology, Columbia University, College of Physicians and Surgeons, New York, New York, USA. <sup>6</sup>Division of Integrative Neuroscience, New York State Psychiatric Institute, New York, New York, USA. <sup>7</sup>Division of Molecular Therapeutics, New York State Psychiatric Institute, New York, New York, USA. <sup>8</sup>Present address: National Institute of Mental Health, Office of the Director, Bethesda, Maryland, USA. Correspondence should be addressed to J.A.G. (joshua.gordon@nih.gov) or C.K. (ck491@cumc.columbia.edu).

Received 11 September 2016; accepted 21 April 2017; published online 3 May 2017; corrected online 5 May 2017 (details online); corrected after print 31 May 2018; doi:10.1038/nn.4568

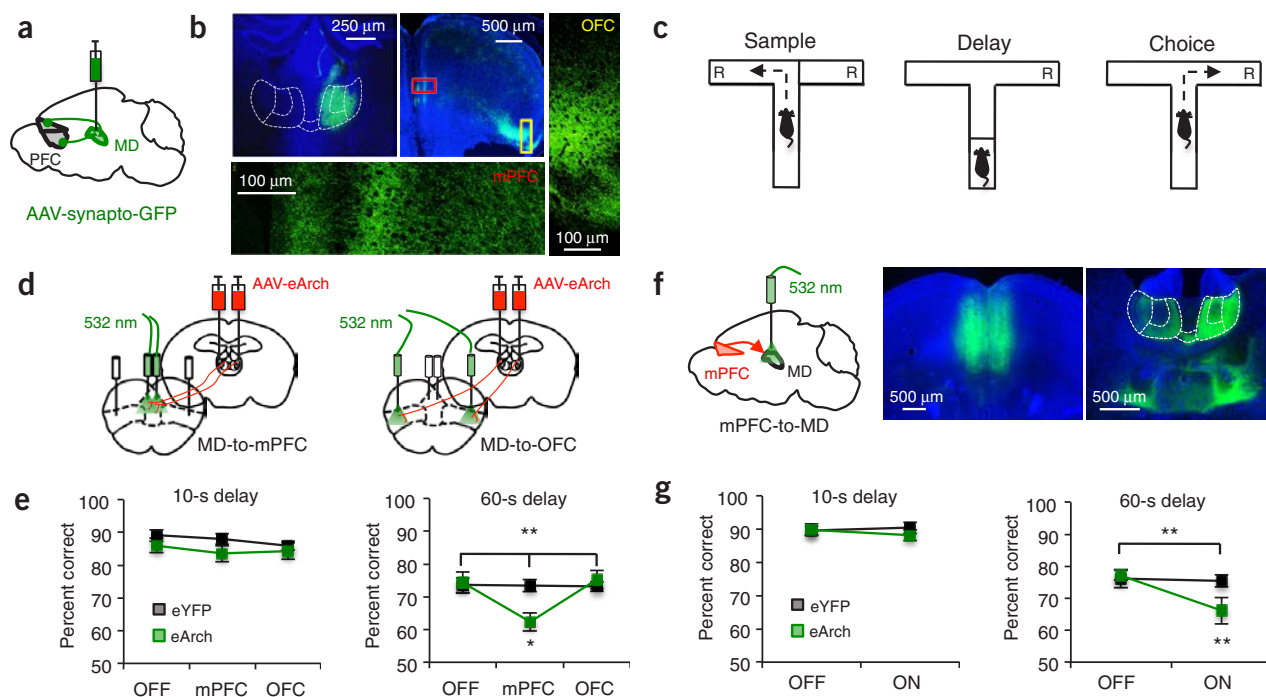


**Figure 1** Reciprocal MD–mPFC activity is required for spatial working memory. (a) Schema of viral delivery of AAV1-CBA-synaptophysin-GFP (AAV-synapto-GFP) for visualization of MD-to-PFC synaptic contacts. (b) Top left: representative expression of synaptophysin-GFP in MD cell bodies. Top middle: synaptophysin-GFP<sup>+</sup> MD terminals in PFC. Bottom and right: confocal images of synaptophysin-GFP<sup>+</sup> MD terminals in mPFC (bottom) and dorsolateral OFC (right). (c) Schema of a single trial of the DNMS T-maze. R, reward locations. (d) Schema of viral delivery of AAV5-hSyn-eArch3.0-eYFP to MD (AAV-eArch) and illumination of MD-to-mPFC (left) or MD-to-OFC (right) terminals within single animals. (e) Percent correct performance in the DNMS T-maze at 10-s (left) or 60-s (right) delays in eYFP (black trace) and eArch-expressing (green trace) mice ( $n = 13$  eYFP, 12 eArch; 10-s data: two-tailed repeated-measures ANOVA (rmANOVA), light  $\times$  group,  $P = 0.67$ ; 60-s data: two-tailed rmANOVA, light  $\times$  group,  $**P = 0.003$ ,  $F_{2,46} = 6.73$ ; two-tailed paired  $t$  test, eArch OFF vs. mPFC,  $*P = 0.02$ ,  $t_{11} = -2.74$ ). (f) Left: schema of viral delivery of eArch-eYFP or eYFP to the mPFC and illumination of mPFC-to-MD terminals. Middle: representative viral expression in mPFC cell bodies. Right: mPFC terminals projecting to the MD (outlined in white and parceled by lateral, central and medial subnuclei). (g) As in e but for mice receiving mPFC-to-MD terminal illumination ( $n = 13$  eYFP mice, 14 eArch mice; 10-s data: two-tailed rmANOVA, light  $\times$  group,  $P = 0.35$ ; 60-s data: two-tailed rmANOVA, light  $\times$  group,  $**P = 0.002$ ,  $F_{1,25} = 12.1$ ; two-tailed paired  $t$  test, eArch light ON vs. OFF,  $**P = 0.001$ ,  $t_{13} = 4.19$ ). Error bars depict s.e.m. throughout.

## RESULTS

### Activity within topographical MD–mPFC connections is required for spatial working memory

While the anatomy of MD–prefrontal circuitry is well described in primates<sup>19</sup> and rats<sup>20,21</sup>, there have been comparatively fewer anatomical studies in the mouse. We therefore first sought to extend this literature by closely examining thalamo–prefrontal connectivity in the mouse. Using virally mediated synaptophysin-GFP expression to visualize MD terminals, we observed that the mouse MD makes extensive synaptic connections with multiple prefrontal areas, with particularly dense terminations in the mPFC and orbitofrontal cortex (OFC; Fig. 1a,b).

To identify the MD substructures anatomically associated with these PFC regions in the mouse, we delivered the dual anterograde and retrograde tracers fluoro-emerald and fluoro-ruby to either the OFC or mPFC (Supplementary Fig. 1a,b). We found minimal overlap in both the terminal fields of PFC projections to the MD and MD neurons with projections back to the medial and orbital walls of the PFC (Supplementary Fig. 1c). That is, while mPFC neurons primarily projected to and received input from the lateral and medial MD, OFC neurons predominately projected to and received input from the central MD (Supplementary Fig. 1d). Although our injections did not distinguish between dorsal and ventral aspects of mPFC, we generally observed denser connectivity with lateral MD when dorsal mPFC was densely labeled and denser connectivity with medial MD when ventral mPFC was densely labeled. As recently reported in the mouse<sup>22</sup>, this reflects the presence of two distinct and topographically organized

MD–mPFC circuits. This topographic and reciprocal MD–PFC organization is consistent with anatomical findings in primates<sup>19</sup> and rats<sup>20,21</sup>.

Previous findings suggested that mPFC is the prefrontal region most relevant to spatial working memory on a delayed nonmatch-to-sample (DNMS) ‘win-shift’ T-maze, in which mice have to choose a spatial location that differs from the one they randomly sample before a delay period<sup>23,24</sup> (Fig. 1c). We previously demonstrated that this task also relies on MD activity<sup>10</sup>. We therefore hypothesized that activity in MD-to-mPFC projections, but not MD-to-OFC projections, would be required for task performance. To test this hypothesis, we optogenetically inhibited MD terminals alternately in either the mPFC or OFC within the same animals (Fig. 1d). Both regions are sufficiently far apart that light does not spread from one region to another, an observation we independently confirmed by modeling the propagation of light in the mPFC according to our specific optogenetic parameters (Supplementary Fig. 2a). Terminal inhibition was achieved by delivering 532-nm light (10-mW) via flat-tipped optical fibers (200  $\mu$ m, 0.22 NA) to MD terminals expressing the membrane-trafficking-enhanced variant of the proton pump archaerhodopsin (eArch3.0; referred to as eArch hereafter), which we have previously shown is effective for inhibiting vHPC inputs to the mPFC<sup>18,25</sup>. eYFP was used to control for potential effects of light alone<sup>26</sup>. We found a robust impairment of task performance when MD terminals were inhibited within the mPFC for the duration of a trial (Fig. 1e). No effect was observed when MD terminals within OFC were inhibited in an identical manner (Fig. 1e). Notably, this effect was related to delay-phase length, with terminal

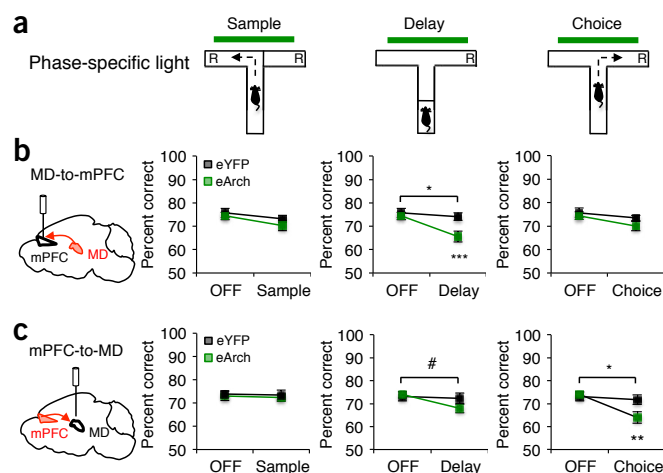


**Figure 2** Discrete task phases depend on distinct MD–mPFC interactions. (a) Schema of terminal illumination (green bar) restricted to the sample, delay or choice phase of the DNMS T-maze. (b) Left: experimental schema. Right: percent correct performance in mice receiving MD-to-mPFC terminal illumination ( $n = 11$  eYFP (black), 17 eArch (green)) during the sample phase (two-tailed rmANOVA, light  $\times$  group,  $P = 0.59$ ), the delay phase (two-tailed rmANOVA, light  $\times$  group,  $*P = 0.016$ ,  $F_{1,26} = 6.7$ ; two-tailed paired  $t$  test, eArch light OFF vs. ON delay,  $***P = 0.0003$ ,  $t_{16} = 4.57$ ) or choice phase (two-tailed rmANOVA, light  $\times$  group,  $P = 0.51$ ). (c) Left: experimental schema. Right: DNMS T-maze performance for mice receiving mPFC-to-MD terminal illumination ( $n = 13$  eYFP (black), 14 eArch (green)) during the sample phase (two-tailed rmANOVA, light  $\times$  group,  $P = 0.94$ ), delay phase (two-tailed rmANOVA, light  $\times$  group,  $\#P = 0.073$ ,  $F_{1,25} = 3.51$ ) or choice phase (rmANOVA, light  $\times$  group,  $*P = 0.02$ ,  $F_{1,25} = 6.62$ ; two-tailed paired  $t$  test, eArch light OFF vs. ON choice,  $**P = 0.002$ ,  $t_{13} = 3.85$ ). Error bars depict s.e.m. throughout.

inhibition only producing deficits under a more demanding long delay (60 s). We previously observed a similar delay-dependent deficit in spatial working memory when inhibiting MD cell bodies<sup>10</sup>. The present results indicate that this finding is due to the inhibition of MD neurons projecting to the mPFC but not those projecting to the OFC.

Given the dense reciprocal connectivity between the mPFC and the MD (Supplementary Fig. 1d), we next asked whether mPFC projections to MD were also necessary for working memory performance. We therefore virally expressed eArch or eYFP in mPFC and implanted optical fibers over mPFC terminals in the MD. Inhibiting the mPFC-to-MD projection diminished task performance in a manner that depended on delay-phase length, similarly to inhibition of the reciprocal MD-to-mPFC projection (Fig. 1f,g). These results demonstrate involvement of reciprocal MD–mPFC circuits in spatial working memory and raise the possibility that activity in these circuits could work in concert to support task performance.

### Different task phases require distinct functional interactions between mPFC and MD

To understand the precise manner by which mPFC and MD connections engage in working memory, we first performed temporally limited optogenetic inhibition of MD terminals in mPFC (MD-to-mPFC) and mPFC terminals in MD (mPFC-to-MD) during specific phases of the task. In these experiments, we restricted the delay phase length to the 60-s condition, and terminal inhibition was limited alternately to the sample, delay or choice phase of the task (Fig. 2a). Inhibiting MD-to-mPFC during the sample or choice phases did not significantly impact performance (Fig. 2b). In contrast, MD-to-mPFC inhibition during the delay phase substantially diminished performance, an effect not seen

with optical illumination in the absence of eArch (Fig. 2b). This effect was also unrelated to the disparity between task-phase lengths, as limiting delay-inhibition to 17 s (equivalent to the average sample phase duration) was also sufficient to impair behavioral performance (Supplementary Fig. 3). Our sample sizes (phase-specific inhibition:  $n = 17$  eArch mice, eYFP 11 mice; 17-s inhibition:  $n =$  eArch 16 mice, eYFP 12 mice) were a priori sufficiently powered to detect significant interactions based on our previously observed effect size when inhibiting vHPC inputs to the mPFC during the sample phase (ANOVA, virus  $\times$  light interaction,  $F = 5.92$ ,  $P = 0.02$ ,  $n = 8$  eArch<sup>+</sup> mice, 6 eArch<sup>−</sup> mice)<sup>18</sup>. However, given the nonsignificant tendencies for a decrease in performance when inhibiting MD inputs to the mPFC during the sample phase (phase-specific inhibition:  $P = 0.59$ ,  $\beta = 0.91$ ; 17-s inhibition:  $P = 0.21$ ,  $\beta = 0.73$ ), we cannot exclude the possibility of a Type II error if the true effect size is smaller than predicted. Regardless, these results strongly indicate that activity in the MD-to-mPFC pathway is particularly required during the delay phase, potentially supporting the maintenance of working memory.

To investigate whether mPFC-to-MD engagement in the task was symmetrical to that of the MD-to-mPFC pathway, we performed temporally limited inhibition of this pathway during prescribed phases of the task. We found that, while sample-phase inhibition had no effect on behavior, delay-phase inhibition led to diminished task performance that approached statistical significance ( $P = 0.073$ ,  $\beta = 0.53$ ; Fig. 2c). Strikingly, choice-phase inhibition robustly impaired task performance (Fig. 2c), despite the brief duration of inhibition received (Supplementary Fig. 3a). These asymmetric effects suggest that MD–mPFC pathways are differentially engaged in the task. Specifically, while the MD-to-mPFC pathway is required during the delay phase, possibly in support of working memory maintenance, the mPFC-to-MD pathway may also be required, but to a lesser degree. In contrast, mPFC-to-MD dependence during spatial choice indicates that the MD may function as an output station for mPFC to exert its impact on working memory retrieval, action execution or both. As our manipulations impacted the entire MD and both ventral and dorsal mPFC (Supplementary Fig. 2), which share reciprocal connections with medial and lateral MD, respectively<sup>22</sup>, it is possible that these asymmetric effects may be attributable to topographically discrete MD–mPFC circuits.

The asymmetric effects on working memory performance obtained by MD-to-mPFC inhibition compared to mPFC-to-MD suggested that functional interactions between these circuits are directional and may vary in a task-phase-dependent manner. To directly test this prediction, we analyzed data from simultaneous electrophysiological recordings of mPFC single units and MD local field potentials (LFPs) during the task (Fig. 3a). We used a lag analysis of mPFC units that were significantly phase-locked (Bonferroni-corrected Rayleigh's circular test,  $P < 0.0024$ ) to filtered MD beta oscillations (13–30 Hz) to estimate the net direction of information flow between the two structures (Fig. 3b). During the sample phase, when inhibition of either circuit had no effect on behavior, there was no net directionality between the MD and mPFC (Fig. 3c, i,ii). During the delay phase, however, MD activity led mPFC activity. This directionality suggests a predominance of MD-to-mPFC influence during this phase, consistent with the behavioral impairment seen with MD-to-mPFC terminal inhibition (Fig. 3d, i,ii). Finally, during the choice phase, mPFC activity led MD activity, a result also in line with the behavioral impact of inhibiting this pathway (Fig. 3e, i,ii). Notably, this pattern of net information flow was also observable when performing a lag analysis on cross-correlations of the instantaneous amplitudes of filtered MD and mPFC LFPs<sup>27</sup> (Supplementary Fig. 4a). While LFP–LFP cross-correlations indicated no net direction flow between MD and mPFC during the sample phase, MD LFPs robustly led those in the mPFC during the delay phase, and mPFC LFPs predominately led those in MD during the choice phase (Supplementary Fig. 4b–d). Further strengthening the



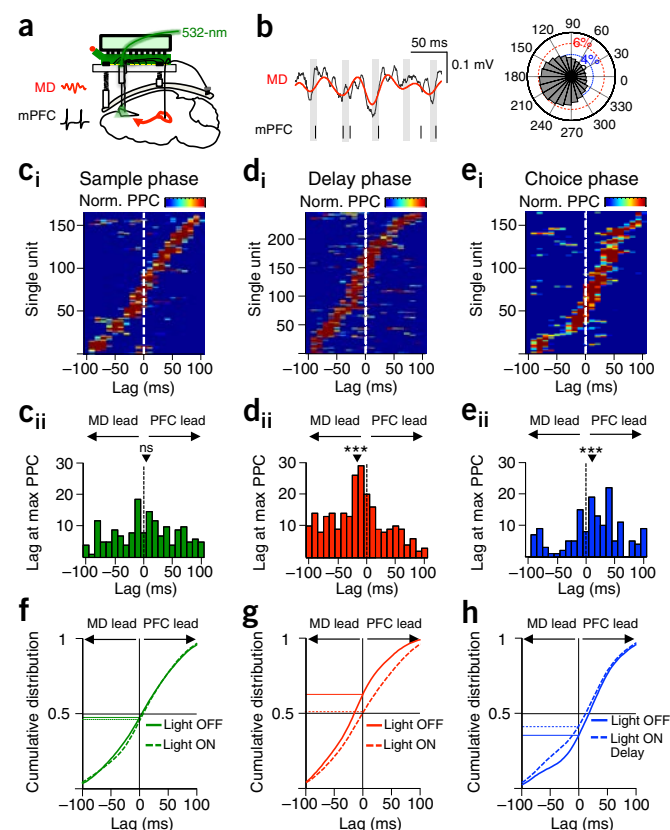


**Figure 3** MD-mPFC functional directionality dynamically shifts across task phases. (a) Schematic of simultaneous recording of MD LFP and mPFC single units. (b) Representative mPFC single unit phase-locked to MD LFP filtered in the beta-frequency range (13–30 Hz). Left: red line depicts filtered beta oscillation overlaid on raw MD LFP (black line). Vertical black lines below indicate simultaneous mPFC spike times; gray shading indicates the trough of the simultaneously recorded MD beta oscillation. Right: polar plot of the distribution of mPFC spikes relative to a single cycle of the MD beta oscillation for the same unit. (c, i) Normalized (norm.) phase-locking values (pairwise phase comparison, PPC) for each mPFC neuron during the sample phase of the DNMS T-maze after shifting mPFC spikes in 10-ms steps over  $\pm 100$  ms. Only mPFC units with peak PPC values meeting Bonferroni-corrected  $P$  values are included (Rayleigh's circular test,  $P < 0.0024$ ; 165 of 547 units). (c, ii) Histogram displaying the lag at which the peak PPC value for each neuron in c, i occurred. Black triangle indicates mean lag value across the population (mean = 3.5 ms; two-tailed signed-rank test, nonsignificant (n.s.):  $P = 0.38$ ;  $z_{165} = 0.88$ ). (d, i, ii) As in c, i, ii but for significantly phase-locked units in the delay phase (246 of 547 units; mean =  $-14.8$  ms; two-tailed signed-rank test,  $***P = 0.000005$ ;  $z_{246} = -4.58$ ). (e, i, ii) As in c, i, ii but for significantly phase-locked units in the choice phase (153 of 547 units; mean = 13.3 ms; two-tailed signed-rank test,  $***P = 0.0002$ ;  $z_{153} = 3.68$ ). (f) Cumulative distribution of significantly phase-locked units during the sample phase across lag times. Solid green curve indicates light OFF trials and dotted green curve indicates light ON sample trials (two-sample Kolmogorov-Smirnov test; n.s.,  $P = 0.98$ ;  $k = 0.049$ ). Horizontal black line indicates 50% proportion; vertical black line indicates lag time of 0. Horizontal green lines indicate the proportion of units exhibiting peak PPC values at negative lag times during light OFF trials (solid line) and during light ON sample trials (dashed line). (g) As in f but for significantly phase-locked units during the delay phase on light OFF trials (solid red curve) and light ON delay trials (dotted red curve; two-sample Kolmogorov-Smirnov test;  $*P = 0.01$ ;  $k = 0.14$ ). (h) As in f but for significantly phase-locked units during the choice phase on light OFF trials (solid blue curve) and light ON delay trials (dotted blue curve; two-sample Kolmogorov-Smirnov test; n.s.,  $P = 0.28$ ;  $k = 0.11$ ).

links between these observations and our behavioral results, we found that MD-to-mPFC terminal inhibition during the sample phase had no effect

on the net directionality of phase-locking between structures (Fig. 3f), while delay-phase terminal inhibition diminished MD leading activity during the delay (Fig. 3g), although not during the subsequent spatial choice (Fig. 3h). Together, these findings support the conclusion that during the delay phase, mPFC is dependent on functional MD input for the maintenance of working memory, while during the subsequent choice phase, mPFC outputs to the MD guide the retrieval and/or action execution of successfully maintained working memory plans.

### mPFC neurons show elevated spiking during the delay but no spatial tuning

Having obtained recordings from multiple mPFC single units during the task, we interrogated their spiking across task phases to determine which task variables they encoded and when. Consistent with our prior results<sup>18</sup> and those of others<sup>28</sup>, we found that many mPFC neurons were spatially tuned toward one maze location over another during both the sample and choice phases (Fig. 4). This was clearly observed in both single-unit examples (Fig. 4b) and across the entire population of mPFC units (Fig. 4c, i–iii), with spatial tuning in individual neurons largely overlapping between sample and choice phases (Fig. 4c, iii). In contrast, we found no evidence for spatial tuning during the delay phase, whether analyzed by which arm was visited during the preceding sample phase (Fig. 4c, ii) or by which arm was chosen during the subsequent choice phase (Fig. 4, ii). Moreover, spatial tuning was not altered by concurrent MD terminal inhibition during the sample and delay phases (Fig. 4d, i, ii), nor was it affected during the choice phase following inhibition during the preceding delay phase (Fig. 4d, iii). The same effect was observed when we restricted our analyses to only neurons that were significantly spatially tuned (Supplementary Fig. 5). Notably, these results were not due to a failure of terminal inhibition, as eArch activation produced substantial modulations in mPFC firing rates compared to light illumination without eArch (Supplementary Fig. 6). These findings confirm previous observations that in rodents, mPFC neurons do not represent goal arm locations in sustained firing during the delay phase of T-maze tasks<sup>18,28</sup> and further demonstrate that spatial representations of arm locations in mPFC neurons are not dependent on MD-to-mPFC activity.

We reasoned that, while mPFC neurons do not explicitly encode spatial location during the delay phase, they may represent other variables critical for task performance. Consistent with this, we found a subset of mPFC neurons (266 of 891) that exhibited significant elevations in spiking during the delay relative to the intertrial interval (ITI;  $z > 2$ ,  $P < 0.05$  for 2 or more consecutive 1-s bins), in which behavioral conditions were equivalent but mice were not required to maintain a working memory trace. Elevations in spiking for each neuron were not sustained; rather, each neuron exhibited a preferred temporal offset during the delay phase (Fig. 5a). As a population, this activity pattern tiled the entire delay phase, and semiautomated clustering of the data based on temporal correlations in firing revealed a Poisson-like distribution pattern characterized by a gradual decay and broadening of clustered subpopulation peaks as the delay period progressed (Fig. 5b, i). This pattern was not observed in a largely mutually exclusive group of mPFC neurons identified as having significantly suppressed delay activity (260 of 891), in which the vast majority of peak suppression occurred within the first five seconds of the delay ( $z < -2$ ,  $P < 0.05$  for 2 or more consecutive 1-s bins; 201 of 260; Supplementary Fig. 7). Moreover, shuffled versions of the entire dataset both significantly reduced the number of neurons exhibiting delay-elevated activity and abolished the unique temporal structure of delay-elevated clusters (Fig. 5b, ii, iii). These findings were replicated in an independent dataset of mPFC single units (Fig. 5c, d), and together they indicate that delay-elevated neurons were not artifacts created by

spiking on a small number of trials and that the observed firing pattern of clustered data did not emerge by chance.

Temporally sparse and sequential activation of neural ensembles have previously been reported in rodents performing tasks assessing both working memory and interval timing<sup>29–33</sup>. To assess whether delay-elevated mPFC neurons represented information related to interval timing, we recorded single units in the mPFC in mice performing the T-maze at two distinct delays, 60 s and 20 s. In contrast to previous findings that time-coding neural populations scale their activity according to interval durations<sup>32</sup>, we found that only delay-elevated neurons with peaks in the first 20 s of the 60-s delay retained their temporal preference during the shorter 20-s delay (**Supplementary Fig. 8**). We therefore hypothesized that delay-elevated mPFC activity may reflect the maintenance of a working memory-related representation across the delay phase. If true, we reasoned that delay-elevated activity should be attenuated on incorrect trials. Indeed, we observed diminished spiking in delay-elevated neurons in normalized firing rates across individual neurons (**Fig. 6a, i**), across clustered subpopulations (**Fig. 6a, ii**), in raw data examples (**Fig. 6a, iii**) and in the ratio of incorrect/correct firing in neurons grouped by distinct temporal offsets (**Fig. 6d, i**).

Given that MD input during the delay phase was necessary for task performance, we next asked whether they were also important for delay activity in the mPFC. Notably, MD terminal inhibition throughout the delay had temporally specific effects on mPFC delay firing. While delay-elevated firing in clusters with early temporal offsets were largely left intact, firing rates in middle and late clusters were substantially diminished (**Fig. 6b, i–iii** and **Fig. 6d, ii**). These results are not explained by an effect of light alone, as they were not observed in eYFP animals (**Supplementary Fig. 9**). Moreover, these findings are also not due to a nonspecific effect of removing excitatory drive to mPFC neurons, as terminal inhibition of vHPC inputs to the mPFC during the delay had no impact on delay-elevated firing (**Fig. 6c, i–iii** and **Fig. 6d, iii**). Indeed, the MD-dependence of delay-elevated mPFC activity was notably input- and task-phase specific. While activity in delay-elevated neurons was suppressed by MD terminal inhibition during the delay phase (**Fig. 7a, i,ii**), activity in this same population was unaffected by MD terminal inhibition during the sample phase (**Fig. 7a, ii**). Moreover, these neurons were also not impacted by vHPC terminal inhibition in either sample or delay phases (**Fig. 7b, i,ii**). These results suggest that MD inputs were specifically critical for sustaining delay-elevated mPFC representations across the delay phase. Strengthening this notion, the largely non-overlapping group of spatially tuned mPFC neurons (**Supplementary Fig. 7b**) exhibited activity dependence on vHPC inputs during the sample phase (**Fig. 7b, iii**) but were independent of MD inputs in both sample and delay phases (**Fig. 7a, iii**). Together, these results reveal a double dissociation of the MD-dependence and vHPC-dependence of delay-elevated and spatially tuned mPFC neurons, respectively. Strikingly, the two populations only depend on their respective inputs when modulated by the task phase in which they are feature-selective.

If delay-elevated mPFC neurons represent task-relevant information that is exclusively dependent on MD inputs for their maintenance across the delay phase, we reasoned that facilitating MD activity should improve behavioral performance in a task-phase-specific manner. To test this idea, we used a stabilized-step-function opsin (SSFO), which is capable of broadly enhancing neural excitability in a temporally restricted manner without explicitly controlling spike timing<sup>34</sup>. As such, we virally delivered SSFO (via AAV2-CamKIIa-SSFO-mCherry) to the MD, bilaterally implanted fiber optics dorsal to it and activated SSFO exclusively during either the sample or delay phases in mice performing the DNMS T-maze. Strikingly, we found that enhancing MD excitability during the delay phase but not the sample phase of the task improved

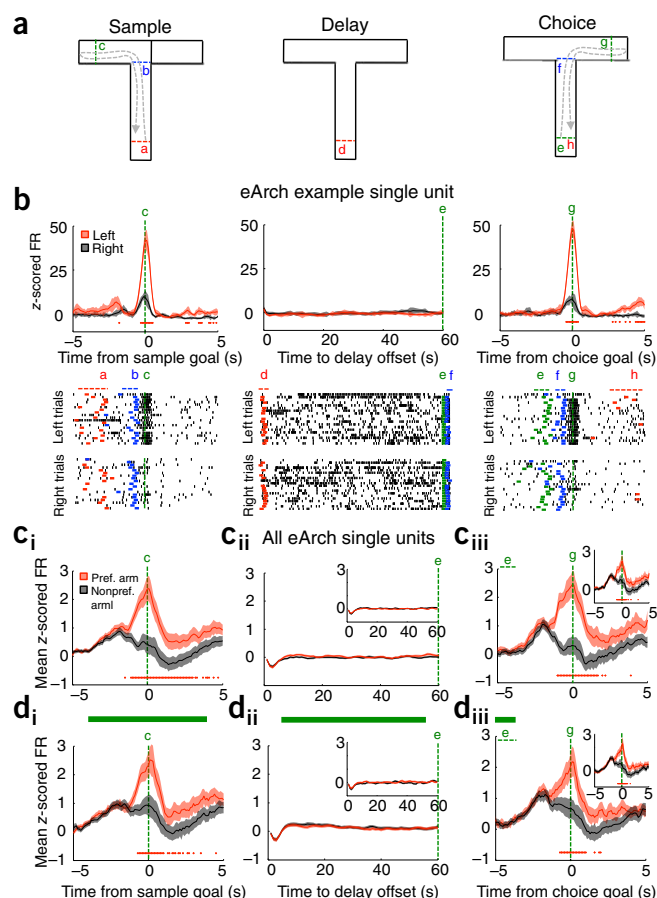


**Figure 4** mPFC spatial tuning is absent during the delay phase and independent of MD input. (a) Schema of behavioral timestamps for spike alignment on a single DNMS T-maze trial. (b) Example mPFC single unit spatially tuned to left-arm runs. Top: perievent normalized spike rates on left arm (red trace) or right arm (black trace) trials (100-ms bins for sample and choice; 1-s bins for delay). Bottom: raster plots of raw spike times on left and right trials. Colored lines and letters in raster plots display trial-by-trial event timestamps indicated in a. (c) Normalized firing rates on light OFF preferred-arm trials (red trace) or light OFF nonpreferred-arm trials (black trace) averaged across all eArch single units ( $n = 891$  units from 9 eArch mice). Arm preference was determined from firing rate differences on sample arm runs (i–iii) or choice arm runs (insets in ii and iii). (d) As in c, but for trials in which MD-to-mPFC terminals were inhibited (green bar) during the sample (i) or delay (ii and iii) phases. In all normalized firing rate plots, red asterisks indicate bins with two-tailed Wilcoxon signed-rank (population comparison) or two-tailed Wilcoxon rank-sum (single-unit comparison) significance at Bonferroni-corrected  $P$  values ( $P < 0.0005$  sample and choice;  $P < 0.00083$  delay). Error bars depict s.e.m. throughout.

behavioral performance (**Fig. 7c**). This finding is consistent with a specific role for MD inputs in sustaining delay-elevated mPFC activity without impacting mPFC spatial encoding during the sample phase and provides further evidence that MD-dependent delay-elevated mPFC activity supports the maintenance of working memory representations critical for task performance.

## DISCUSSION

Here we demonstrated that reciprocal MD–mPFC activity was required for spatial working memory in mice (**Fig. 1**). By dissecting the role of each reciprocal projection during discrete task phases of the DNMS T-maze, we further revealed that while MD inputs to the mPFC supported the maintenance of working memory, mPFC inputs to the MD supported the

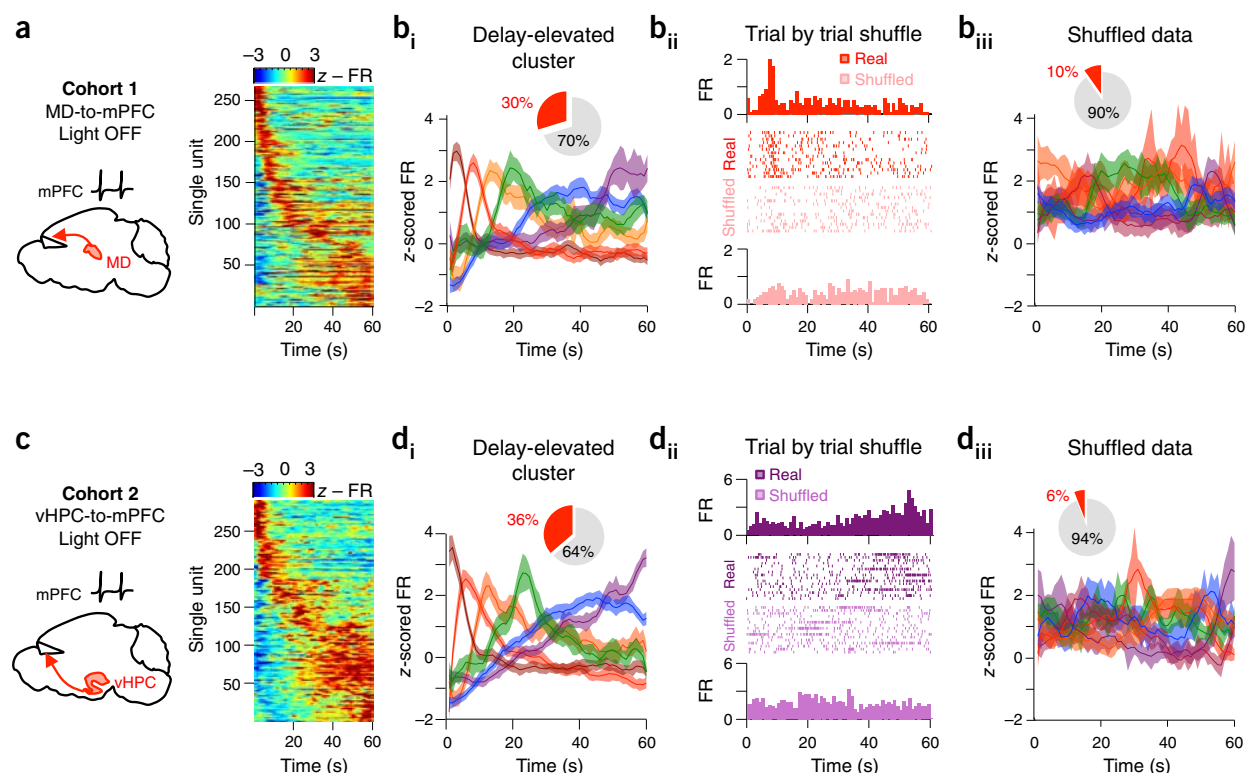


**Figure 5** Delay-elevated mPFC neurons exhibit temporally sparse and sequential activity that tiles the delay phase. **(a)** Left: experimental schema. Right: normalized firing rates during the delay phase of the DNMS T-maze in a subpopulation of mPFC single units that exhibit significant elevations in delay period activity (266 of 891 units from a cohort of 9 mice expressing eArch in the MD). Normalized firing rates were averaged across all light OFF trials. Single units were then sorted by time of peak firing rate. **(b, i)** Mean z-scored firing rate of delay-elevated units identified in **a** after clustering into six groups based on temporal correlation in firing rates from dark red (earliest) to purple (latest). Inset: proportion of all mPFC neurons in the dataset that exhibited significant delay-elevated activity (red slice, 30%). **(b, ii)** Time-triggered histogram and trial-by-trial raster plot of an example delay-elevated mPFC unit. Histograms and rasters of raw spikes from real data (top) and shuffled versions of the data (bottom) are shown. **(b, iii)** Delay-elevated neurons identified as in **a** and clustered as in **b, i** but from a trial-by-trial shuffled version of the entire dataset. Inset: proportion of all mPFC neurons in the shuffled dataset that exhibit significant delay-elevated activity according to criterion used in **a** (88 of 891 units, 10%). **(c)** As in **a** but for mPFC units obtained from an independent cohort of 6 mice expressing eArch in the vHPC. **(d, i–iii)** As in **b** but for mPFC units obtained from an independent cohort of 6 mice expressing eArch in the vHPC. Inset in **i**: 290 of 800 units (36%) exhibit delay-elevated activity according to criterion in **a**. Inset in **iii**: 47 of 800 units exhibit delay-elevated activity following trial-by-trial shuffling of the entire dataset, as in **b, iii**. Example single units are colored according to their clustered group in **b, i** and **d, i**, respectively.

retrieval of memory for action execution (Fig. 2). We corroborated this model using two distinct directionality analyses of simultaneous mPFC and MD activity, which both revealed a dynamic shift from MD-led activity during the delay phase toward mPFC-led activity during the choice phase (Fig. 3 and Supplementary Fig. 4). Finally, we uncovered a population of mPFC neurons whose activity was temporally sparse within individual neurons and sequential across the population (Fig. 5). This activity pattern indicated correct performance and depended on MD inputs, but not vHPC inputs, for sustained maintenance across the delay (Fig. 6). We further revealed a double-dissociation of the MD-dependence and vHPC-dependence of delay-elevated and spatially tuned mPFC neurons, respectively, a finding that is also specific to the task phase in which each population is feature-selective (Fig. 7). These findings are consistent with a role for MD inputs in sustaining mPFC working memory representations across a delay, a notion supported by improvements in working memory performance when enhancing MD activity during the delay phase but not sample phase of our working memory task (Fig. 7).

What is the nature of the mPFC representation supported by MD input during the delay? The absence of spatial tuning across our mPFC population during the delay (Fig. 4), the largely exclusive nature of spatially tuned and delay-elevated mPFC populations (Supplementary Fig. 7b) and the vHPC-independence of delay-elevated activity (Fig. 7b, i,ii) strongly

argues against the presence of an explicit spatial representation. This finding is unexpected in the context of well-documented observations of spatial tuning in PFC delay-period activity in primates<sup>35–37</sup>. This is typically observed in delayed-response tasks requiring the caching of one spatial location from multiple potential targets. Notably, in a two-choice version of this task analogous to ours, seminal work demonstrating sustained delay period activity in primate PFC also reported that spatial preferences in delay-tuned neurons were either absent<sup>38</sup> or minimal<sup>39,40</sup> (6–13% of sustained delay units). mPFC delay activity did also not appear to encode timing of the delay interval, as delay-elevated mPFC neurons did not scale their activity according to distinct delay durations (Supplementary Fig. 8), a feature observed in neural ensembles explicitly linked to interval timing<sup>32</sup>. Delay-elevated activity may instead reflect a general attentive or task-engaged state. Although our findings do not exclude this possibility, we did not observe overt behavioral differences between correct and incorrect trials, nor was the latency for mice to make a spatial choice altered by MD terminal inhibition (data not shown). A final possibility is that explicit spatial representations are unnecessary for two-choice spatial working memory tasks and that an abstract task rule, such as ‘go to the opposite location’, is sufficient to guide behavioral performance. A direct test of this hypothesis within the context of our task, however, would require that the task rule, and not only the spatial location, vary on a trial-by-trial basis.



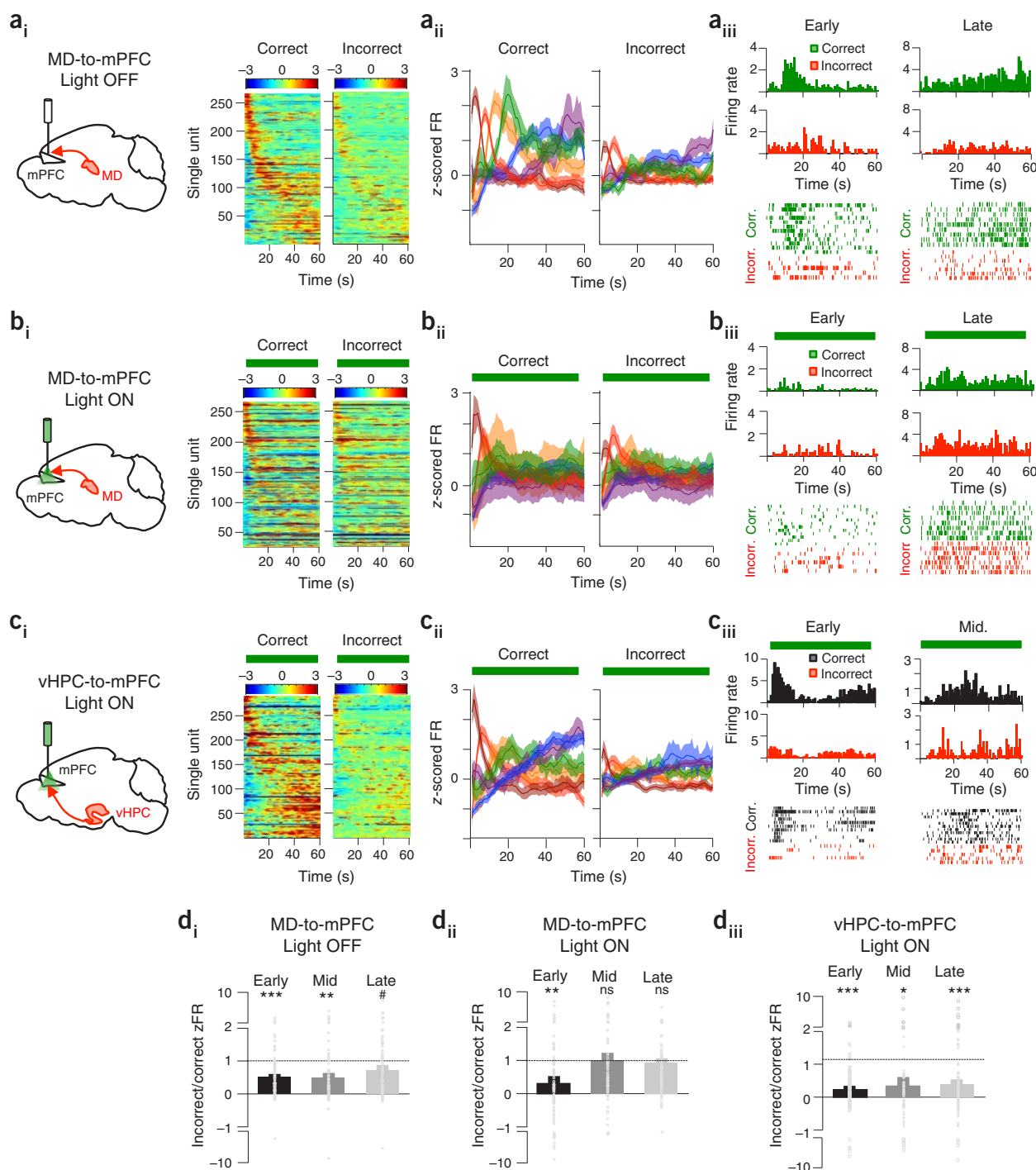


**Figure 6** Delay-elevated mPFC activity is diminished on incorrect trials and selectively depends on MD inputs. (**a, i**) Left: experimental schema. Right: normalized firing rates of delay-elevated mPFC neurons during light OFF trials, parsed by correct or incorrect behavioral performance (266 of 891 units from  $n = 9$  mice expressing eArch in the MD). (**a, ii**) Mean normalized firing rate of delay-elevated units after clustering into six groups based on temporal correlations in firing rates from dark red (earliest) to purple (latest). (**a, iii**) Time-triggered histograms and trial-by-trial raster plots from representative delay-elevated units exhibiting early (left) or late (right) delay peaks. Only spikes from light OFF trials are included, plotted separately for correct (green) or incorrect (red) trials. (**b**) As in **a** but for trials in which MD-to-mPFC inputs were inhibited during the delay phase. The same single units shown in the light off condition in **a, iii** are shown in the MD-to-mPFC light on delay condition in **b, iii**. (**c**) As in **a** but for delay-elevated mPFC units obtained from 6 mice expressing eArch in the vHPC (290 of 800). Only trials in which vHPC-to-mPFC inputs were inhibited during the delay are included. (**d, i**) Ratio of correct/incorrect normalized firing at time of peak firing on all light OFF trials, averaged across units grouped by early (91), middle (83) or late (92) peak times. Groupings reflect the first two, middle two or last two clusters in **a, ii**. Overlaid circles display all individual single units. Significance was determined using a two-tailed  $t$  test against a distribution with a mean of 1 ( $***P < 0.001$ ,  $t_{90} = -5.65$ ;  $**P = 0.0015$ ,  $t_{82} = -3.29$ ;  $\#P = 0.07$ ,  $t_{91} = -1.82$ ). zFR, z-scored firing rate. (**d, ii**) As in **d, i** but for MD-to-mPFC light ON delay trials only ( $**P = 0.003$ ,  $t_{90} = -3.07$ ; not significant (n.s.)). (**d, iii**) As in **d, i** but for vHPC-to-mPFC light ON delay trials only ( $***P < 0.001$ ,  $t_{102} = -6.24$ ;  $*P = 0.018$ ,  $t_{64} = 2.42$ ;  $***P = 0.0001$ ,  $t_{121} = -3.97$ ). Error bars depict s.e.m. throughout.

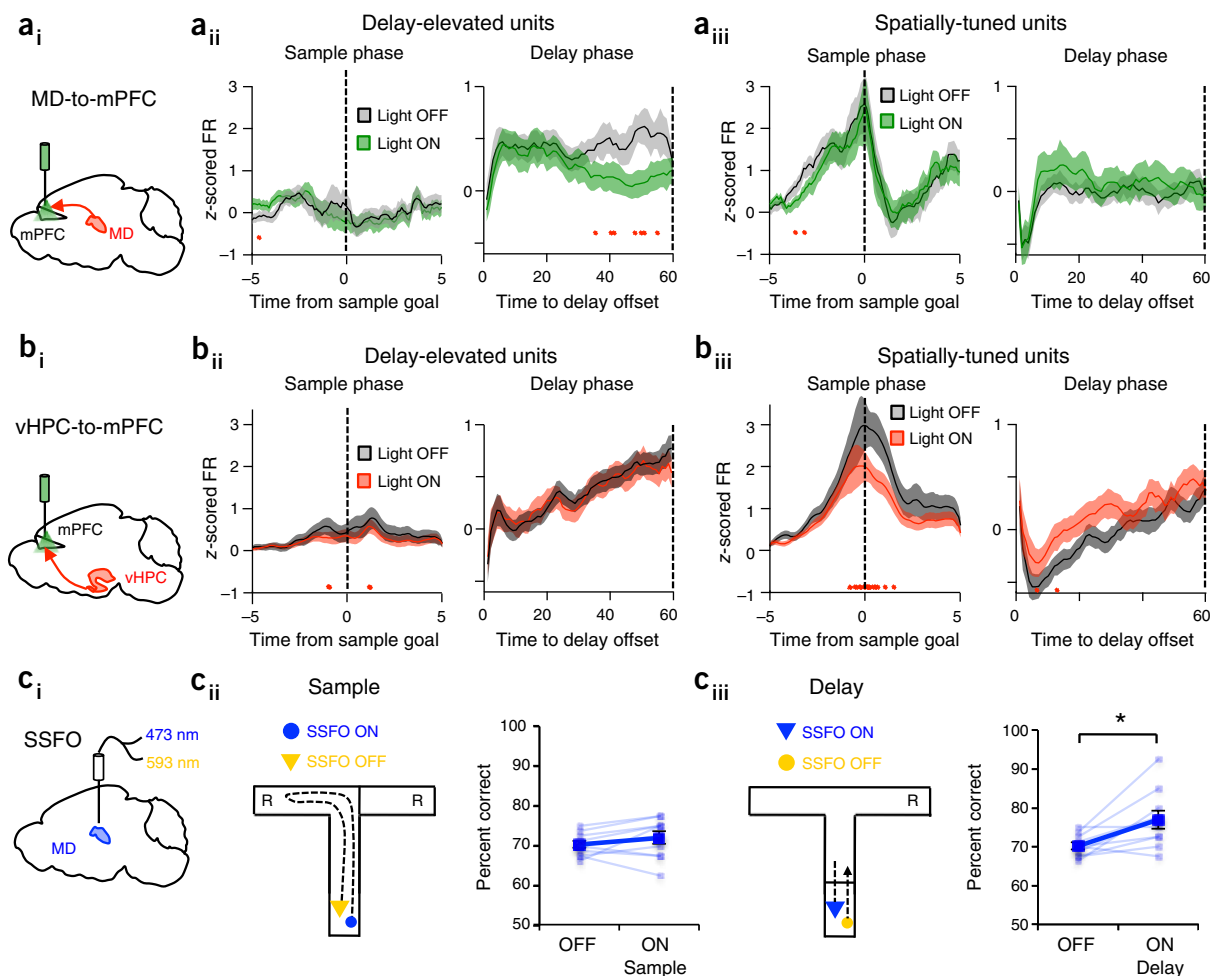


**Figure 7** MD activity sustains mPFC delay activity in an input and task phase specific manner. **(a)** Experimental schema **(i)** and normalized firing rates in delay-elevated **(ii; 266 of 891 units)** and spatially tuned **(iii; 250 of 891 units)** mPFC neurons obtained from 9 mice expressing eArch in the MD and receiving task-phase specific MD-to-mPFC inhibition during either the sample or delay phases of the DNMS T-maze. Only correct trials are included, parsed by light OFF (black trace) or light ON (green trace) conditions. Red asterisks denote bins with Wilcoxon signed-rank significance ( $P < 0.0005$  sample and choice;  $P < 0.00083$  delay). **(b)** As in **a** but for mPFC neurons obtained from 6 mice expressing eArch in the vHPC (800 units) and receiving task-phase specific vHPC-to-mPFC inhibition. Delay-elevated, 290 of 800 units; spatially tuned, 250 of 800 units. **(c, i)** Schema of SSFO (hChr2(C128S/D156A)) activation and deactivation of MD activity. **(c, ii)** Schema of SSFO activation at sample-phase onset and deactivation at sample-phase offset (left). Percent correct performance in the DNMS T-maze in 9 SSFO-expressing mice during light OFF and ON sample trials (right). Transparent blue lines show individual mouse performance; thick blue line indicates group mean performance (two-tailed paired  $t$  test:  $P = 0.26$ ;  $t_8 = -1.22$ ). **(c, iii)** As in **c, ii** but for mice receiving SSFO activation of the MD at delay onset and deactivation at delay offset (two-tailed rmANOVA on all trial types, light effect:  $P = 0.004$ ,  $F_7 = 7.75$ ; two-tailed paired  $t$  test, light OFF vs. ON delay:  $P = 0.014$ ,  $t_8 = -3.14$ ). Error bars depict s.e.m. throughout.

Nevertheless, task-rule encoding in PFC neurons has been frequently reported in both rodents<sup>41,42</sup> and primates<sup>43,44</sup>. Moreover, findings from a recent working-memory-guided, top-down attention task, in which task rules are varied on a trial-by-trial basis, explicitly demonstrate task-rule encoding in mouse mPFC neurons during the delay period<sup>45</sup>. Like the delay-elevated mPFC activity in our task, this study observes temporally sparse and sequential mPFC spiking coding for one of two task rules during the delay period. Notably, and further strengthening our inference, delay-elevated activity in this task requires MD activity for its sustained maintenance across the delay. Our results make clear that this effect is due to activity in MD-to-mPFC projections and not to alterations in general excitability.

The parallels between our findings and those of Schmitt *et al.*<sup>45</sup> are quite striking when considering the difference in temporal scale between tasks. The fact that our population of mPFC neurons was

capable of spanning a 60-s delay may indicate a fundamental scalability of mPFC encoding and maintenance of rule representation across time scales. In this light, our findings extend studies that have identified sequential activation of cortical neurons in tasks that require working memory<sup>29–31</sup> and support the idea that sequences of activation may be a common circuit function in memory-guided decision tasks. It is also noteworthy that we observed a gradual degradation in the quality of elevated spiking across time (Fig. 5a,b). This is evocative of a decay in prefrontal representation and may explain why our MD-mPFC manipulations did not impact behavior at shorter delays (Fig. 1e,g), in which delay representations were potentially robust to activity disruptions in our task. Furthermore, and consistent with this interpretation, mPFC delay activity with early peak times was unaffected by MD terminal inhibition (Fig. 6b,d, ii and Fig. 7a, ii). Local PFC circuitry may therefore be sufficient to maintain representations at short time-scales but



may require amplification for sustained maintenance either as memory decays across time or in more cognitively demanding tasks.

How does the mPFC-to-MD pathway support working memory performance? Our terminal-inhibition experiments and directionality analyses both indicate a critical role for this pathway during the choice phase of our task, when mice presumably needed to retrieve maintained information and translate it to motor action (Fig. 2c and 3e, i,ii and Supplementary Fig. 4). Although this finding may suggest an unexpected functional dissociation with the reciprocal MD-to-mPFC pathway, this interpretation warrants substantial caution. Our pathway-specific experiments did not distinguish between dorsal and ventral mPFC (Supplementary Fig. 2), which reciprocally connect with lateral and medial MD, respectively, in a largely segregated manner<sup>21,22</sup>. It is therefore possible that the distinct phase-specific behavioral impairments we observed may be attributable to activity in discrete MD–mPFC circuits, a possibility that will be important to resolve in future research. Nevertheless, this observation does suggest that the lateral and/or medial MD may serve as an intermediate output pathway for mPFC to recruit downstream motor planning circuits. Indeed, the mPFC has been shown to exert strong functional control over primary motor cortex<sup>46</sup>, and higher order thalamic nuclei like the MD are posited to play a role in information transfer between cortical areas<sup>6,47</sup>. While anatomical connectivity exists between MD and the primary and secondary motor cortex<sup>48,49</sup>, the behavioral functions of these circuits remain entirely unexplored. An alternative possibility is that mPFC-to-MD circuits may be important for cortical or subcortical pathways involved in memory retrieval. Future efforts to expand functional circuit dissection of MD–PFC pathways and their associated structures with increasing precision could provide answers to these important questions.

In the context of our previous studies inhibiting vHPC-to-mPFC inputs<sup>18</sup>, our results provide a striking example of differential long-range circuit engagement in the DNMS T-maze. Here we observed a limited impact of MD terminal inhibition when inhibition was restricted to the sample phase of the task and a robust behavioral impairment when inhibition was restricted to the delay phase (Fig. 2b and Supplementary Fig. 3). In contrast, vHPC terminal inhibition robustly impairs behavioral performance during the sample phase but not the delay phase<sup>18</sup>. Extending this dissociation further, we reveal here a double dissociation in the MD-dependence and vHPC-dependence of delay-elevated and spatially tuned mPFC neurons (Fig. 7a,b). This finding demonstrates a functional dissociation of prefrontal substrates for working memory encoding and maintenance in the DNMS T-maze task. Our results suggest this dissociation is largely due to the segregation of spatially tuned and delay-elevated mPFC neurons into largely non-overlapping populations (Supplementary Fig. 7b).

Our findings should have translational relevance, particularly to schizophrenia. Patients with schizophrenia exhibit prefrontal-associated cognitive deficits in domains such as executive function and working memory, and neuroimaging studies increasingly report diminished thalamo–prefrontal connectivity in such patients<sup>15–17</sup>. Our data provide clear evidence that these circuit abnormalities are likely to be causally involved in producing working memory deficits. Continued investigation of thalamo–prefrontal interactions in different behavioral conditions in patients and in animal models will be critical for advancing clinical efforts for improved diagnoses and more targeted therapeutic approaches<sup>50</sup>.

## METHODS

Methods, including statements of data availability and any associated accession codes and references, are available in the [online version of the paper](#).

*Note: Any Supplementary Information and Source Data files are available in the online version of the paper.*

## ACKNOWLEDGMENTS

We thank members of the Gordon and Kellendonk labs for technical assistance and discussions. We also thank M. Halassa for discussions and commentary on an initial draft of the manuscript. This work was supported by grants from the NIMH (R01 MH096274 to J.A.G., F31 MH102041 to S.S.B. and F30 MH107204 to J.M.S.); by the Hope for Depression Research Foundation (to J.A.G.); and by the Irma Hirschl Trust (to C.K.). This article was prepared while J.A.G. was employed at the Department of Psychiatry at Columbia University and NYSPI. The opinions expressed in this article are the author's own and do not reflect the view of the National Institutes of Health, the Department of Health and Human Services or the United States government.

## AUTHOR CONTRIBUTIONS

S.S.B., J.A.G. and C.K. designed the experiments. S.S.B. performed the experiments and analyzed the data. J.M.S., S.P., T.J.S., C.R., A.I.A. and A.Z.H. assisted in the design, performance, analysis and interpretation of experiments. S.S.B., J.A.G. and C.K. interpreted the results and wrote the paper.

## COMPETING FINANCIAL INTERESTS

The authors declare no competing financial interests.

Reprints and permissions information is available online at <http://www.nature.com/reprints/index.html>. Publisher's note: Springer Nature remains neutral with regard to jurisdictional claims in published maps and institutional affiliations.

1. Fuster, J.M. *The Prefrontal Cortex. Anatomy, Physiology, and Neuropsychology of the Frontal Lobe*. 2nd ed. (Raven, 1989).
2. Minzenberg, M.J., Laird, A.R., Thelen, S., Carter, C.S. & Glahn, D.C. Meta-analysis of 41 functional neuroimaging studies of executive function in schizophrenia. *Arch. Gen. Psychiatry* **66**, 811–822 (2009).
3. Weinberger, D.R. & Berman, K.F. Prefrontal function in schizophrenia: confounds and controversies. *Phil. Trans. R. Soc. Lond. B* **351**, 1495–1503 (1996).
4. Perlstein, W.M., Carter, C.S., Noll, D.C. & Cohen, J.D. Relation of prefrontal cortex dysfunction to working memory and symptoms in schizophrenia. *Am. J. Psychiatry* **158**, 1105–1113 (2001).
5. Mitchell, A.S. The mediodorsal thalamus as a higher order thalamic relay nucleus important for learning and decision-making. *Neurosci. Biobehav. Rev.* **54**, 76–88 (2015).
6. Saalman, Y.B. Intralaminar and medial thalamic influence on cortical synchrony, information transmission and cognition. *Front. Syst. Neurosci.* **8**, 83 (2014).
7. Baxter, M.G. Mediodorsal thalamus and cognition in non-human primates. *Front. Syst. Neurosci.* **7**, 38 (2013).
8. Jones, E.G. *The Thalamus* (2nd Edition). (Cambridge University Press, 2007).
9. Parnadeau, S. *et al.* Mediodorsal thalamus hypofunction impairs flexible goal-directed behavior. *Biol. Psychiatry* **77**, 445–453 (2015).
10. Parnadeau, S. *et al.* Inhibition of mediodorsal thalamus disrupts thalamofrontal connectivity and cognition. *Neuron* **77**, 1151–1162 (2013).
11. Browning, P.G., Chakraborty, S. & Mitchell, A.S. Evidence for mediodorsal thalamus and prefrontal cortex interactions during cognition in macaques. *Cereb. Cortex* **25**, 4519–4534 (2015).
12. Bailey, K.R. & Mair, R.G. Lesions of specific and nonspecific thalamic nuclei affect prefrontal cortex-dependent aspects of spatial working memory. *Behav. Neurosci.* **119**, 410–419 (2005).
13. Byne, W., Hazlett, E.A., Buchsbaum, M.S. & Kemether, E. The thalamus and schizophrenia: current status of research. *Acta Neuropathol.* **117**, 347–368 (2009).
14. Andrews, J., Wang, L., Csernansky, J.G., Gado, M.H. & Barch, D.M. Abnormalities of thalamic activation and cognition in schizophrenia. *Am. J. Psychiatry* **163**, 463–469 (2006).
15. Woodward, N.D., Karbasforoushan, H. & Heckers, S. Thalamocortical dysconnectivity in schizophrenia. *Am. J. Psychiatry* **169**, 1092–1099 (2012).
16. Anticevic, A. *et al.* Characterizing thalamo-cortical disturbances in schizophrenia and bipolar illness. *Cereb. Cortex* **24**, 3116–3130 (2014).
17. Anticevic, A. *et al.* Association of thalamic dysconnectivity and conversion to psychosis in youth and young adults at elevated clinical risk. *JAMA Psychiatry* **72**, 882–891 (2015).
18. Spellman, T. *et al.* Hippocampal-prefrontal input supports spatial encoding in working memory. *Nature* **522**, 309–314 (2015).
19. Ray, J.P. & Price, J.L. The organization of projections from the mediodorsal nucleus of the thalamus to orbital and medial prefrontal cortex in macaque monkeys. *J. Comp. Neurol.* **337**, 1–31 (1993).
20. Groenewegen, H.J. Organization of the afferent connections of the mediodorsal thalamic nucleus in the rat, related to the mediodorsal-prefrontal topography. *Neuroscience* **24**, 379–431 (1988).
21. Alcaraz, F., Marchand, A.R., Courtaud, G., Coutureau, E. & Wolff, M. Parallel inputs from the mediodorsal thalamus to the prefrontal cortex in the rat. *Eur. J. Neurosci.* **44**, 1972–1986 (2016).

22. Mátyás, F., Lee, J., Shin, H.S. & Acsády, L. The fear circuit of the mouse forebrain: connections between the mediodorsal thalamus, frontal cortices and basolateral amygdala. *Eur. J. Neurosci.* **39**, 1810–1823 (2014).
23. Kellendonk, C. *et al.* Transient and selective overexpression of dopamine D2 receptors in the striatum causes persistent abnormalities in prefrontal cortex functioning. *Neuron* **49**, 603–615 (2006).
24. Yoon, T., Okada, J., Jung, M.W. & Kim, J.J. Prefrontal cortex and hippocampus subserve different components of working memory in rats. *Learn. Mem.* **15**, 97–105 (2008).
25. Padilla-Coreano, N. *et al.* Direct ventral hippocampal-prefrontal input is required for anxiety-related neural activity and behavior. *Neuron* **89**, 857–866 (2016).
26. Stuijenske, J.M., Spellman, T. & Gordon, J.A. Modeling the spatiotemporal dynamics of light and heat propagation for *in vivo* optogenetics. *Cell Rep.* **12**, 525–534 (2015).
27. Adhikari, A., Sigurdsson, T., Topiwala, M.A. & Gordon, J.A. Cross-correlation of instantaneous amplitudes of field potential oscillations: a straightforward method to estimate the directionality and lag between brain areas. *J. Neurosci. Methods* **191**, 191–200 (2010).
28. Jung, M.W., Qin, Y., McNaughton, B.L. & Barnes, C.A. Firing characteristics of deep layer neurons in prefrontal cortex in rats performing spatial working memory tasks. *Cereb. Cortex* **8**, 437–450 (1998).
29. Fujisawa, S., Amarasingham, A., Harrison, M.T. & Buzsáki, G. Behavior-dependent short-term assembly dynamics in the medial prefrontal cortex. *Nat. Neurosci.* **11**, 823–833 (2008).
30. Harvey, C.D., Coen, P. & Tank, D.W. Choice-specific sequences in parietal cortex during a virtual-navigation decision task. *Nature* **484**, 62–68 (2012).
31. Baeg, E.H. *et al.* Dynamics of population code for working memory in the prefrontal cortex. *Neuron* **40**, 177–188 (2003).
32. Mello, G.B., Soares, S. & Paton, J.J. A scalable population code for time in the striatum. *Curr. Biol.* **25**, 1113–1122 (2015).
33. Akhlaghpour, H. *et al.* Dissociated sequential activity and stimulus encoding in the dorsomedial striatum during spatial working memory. *Elife* **5**, e19507 (2016).
34. Yizhar, O. *et al.* Neocortical excitation/inhibition balance in information processing and social dysfunction. *Nature* **477**, 171–178 (2011).
35. Goldman-Rakic, P.S. Cellular basis of working memory. *Neuron* **14**, 477–485 (1995).
36. Funahashi, S. Space representation in the prefrontal cortex. *Prog. Neurobiol.* **103**, 131–155 (2013).
37. Rao, S.C., Rainer, G. & Miller, E.K. Integration of what and where in the primate prefrontal cortex. *Science* **276**, 821–824 (1997).
38. Fuster, J.M. Unit activity in prefrontal cortex during delayed-response performance: neuronal correlates of transient memory. *J. Neurophysiol.* **36**, 61–78 (1973).
39. Niki, H. Differential activity of prefrontal units during right and left delayed response trials. *Brain Res.* **70**, 346–349 (1974).
40. Niki, H. Prefrontal unit activity during delayed alternation in the monkey. I. Relation to direction of response. *Brain Res.* **68**, 185–196 (1974).
41. Rich, E.L. & Shapiro, M. Rat prefrontal cortical neurons selectively code strategy switches. *J. Neurosci.* **29**, 7208–7219 (2009).
42. Durstewitz, D., Vitoz, N.M., Floresco, S.B. & Seamans, J.K. Abrupt transitions between prefrontal neural ensemble states accompany behavioral transitions during rule learning. *Neuron* **66**, 438–448 (2010).
43. Wallis, J.D., Anderson, K.C. & Miller, E.K. Single neurons in prefrontal cortex encode abstract rules. *Nature* **411**, 953–956 (2001).
44. Cromer, J.A., Roy, J.E. & Miller, E.K. Representation of multiple, independent categories in the primate prefrontal cortex. *Neuron* **66**, 796–807 (2010).
45. Schmitt, L. I. *et al.* Thalamic amplification of cortical connectivity sustains attentional control. *Nature* <http://dx.doi.org/10.1038/nature22073> (2017).
46. Narayanan, N.S. & Laubach, M. Top-down control of motor cortex ensembles by dorsomedial prefrontal cortex. *Neuron* **52**, 921–931 (2006).
47. Sherman, S.M. & Guillery, R.W. The role of the thalamus in the flow of information to the cortex. *Phil. Trans. R. Soc. Lond. B* **357**, 1695–1708 (2002).
48. Oh, S.W. *et al.* A mesoscale connectome of the mouse brain. *Nature* **508**, 207–214 (2014).
49. Hunnicutt, B.J. *et al.* A comprehensive thalamocortical projection map at the mesoscopic level. *Nat. Neurosci.* **17**, 1276–1285 (2014).
50. Bolkan, S.S., Carvalho Poyraz, F. & Kellendonk, C. Using human brain imaging studies as a guide toward animal models of schizophrenia. *Neuroscience* **321**, 77–98 (2016).

## ONLINE METHODS

**Animals.** All experiments were carried out on male C57/Bl6 male mice purchased from Jackson Laboratory. Mice were aged 7–8 weeks at the start of experiments and housed under a 12-h light–dark cycle in a temperature-controlled environment with food and water available *ad libitum*. For optogenetic experiments, mice were group housed with littermates (5 mice/cage). Mice with implanted microdrives were individually housed. During behavioral training and testing, mice were food-restricted and maintained at 85% of their initial weight. All procedures were done in accordance with guidelines derived from and approved by the Institutional Animal Care and Use Committees at Columbia University and the New York State Psychiatric Institute.

**Surgical procedures.** Mice were first anesthetized with isoflurane and head-fixed in a stereotactic apparatus (Kopf). In anatomical tracing experiments, an AAV1 expressing synaptophysin-eGFP under the chicken  $\beta$ -actin (CBA) promoter was injected unilaterally into the MD at a volume of 0.2  $\mu$ L (0.1  $\mu$ L/min). Four mice were used and results were identical across all four. Viral production was carried out at Columbia University and care areas shared with the laboratory of T. Jessell. Dextran-amine-coupled fluorophore tracers (fluoro-ruby and fluoro-emerald) were obtained commercially (ThermoFisher Scientific) and bilaterally injected into the mPFC or OFC at a volume of 0.4  $\mu$ L (0.1  $\mu$ L/min). Four mice were used and results were identical across all four. In optogenetic inhibition experiments, mice were bilaterally injected in the MD or mPFC with an AAV5 expressing either eYFP alone or an eArch3.0-eYFP fusion construct under the hSynapsin promoter at a volume of 0.25 or 0.35  $\mu$ L, respectively (0.1  $\mu$ L/min). vHPC was targeted with four injection sites per hemisphere at a volume of 0.2  $\mu$ L each (0.1  $\mu$ L/min). In SSFO experiments, AAV2-CaMKIIa-hChR2(C128S/D156A)-mCherry was delivered bilaterally to the MD at a volume of 0.4  $\mu$ L (0.1  $\mu$ L/min). Opsin-expressing virus was obtained commercially from the University of North Carolina Viral Vector Core. Viral and tracer coordinates were as follows (in mm): MD coordinates:  $-1.2$  AP,  $-3.2$  DV skull,  $\pm 0.35$  ML; mPFC coordinates:  $1.75$  AP,  $-1.8$  DV brain,  $\pm 0.4$  ML; vHPC coordinates:  $-3.0$  AP,  $\pm 3.25$ ,  $-4.0$  and  $-1.75$  DV;  $-3.0$  AP,  $\pm 2.5$ ,  $-3.0$  DV;  $-3.0$  AP,  $\pm 3.4$ ,  $-3.0$  DV.

In optogenetic experiments, in the same procedure mice were also bilaterally implanted with flat tipped, ferrule-coupled optical fibers (0.22 NA, 200- $\mu$ m diameter) immediately dorsal to the targeted structure (OFC, mPFC or MD), fixed to the skull with dental cement. Coordinates were as follows, in mm: OFC:  $+2.65$  AP,  $-2.25$  DV skull,  $\pm 1.85$  ML; mPFC:  $+1.75$  AP,  $-1.2$  DV brain,  $\pm 0.4$  ML; and MD:  $-1.2$  AP,  $-2.75$  DV skull,  $\pm 0.25$  ML). Coordinates are relative to bregma (AP, ML) and to skull or brain surface (DV) where specified.

For *in vivo* neurophysiology experiments, mice were implanted with a moveable microdrive consisting of a 32-channel electronic interface board (NeuroNexus), bilateral ferrule-coupled optical fibers (center-to-center distance: 700–800  $\mu$ m) and a single stereotrode bundle. Stereotrodes for recording spikes were made from 13- $\mu$ m tungsten fine wire (California Fine Wire, Grover Beach, CA) and were coupled to the optical fiber such that stereotrode tips were positioned 300–500  $\mu$ m ventral to the fiber tip. The fiber-coupled stereotrode bundle was then unilaterally targeted to the left mPFC. An additional 50- $\mu$ m tungsten wire for recording LFPs was implanted in the left MD and fixed to the skull with dental cement. For LFP signal processing, skull screws placed over the cerebellum and olfactory bulb served as ground and reference, respectively, while spikes were referenced to a local mPFC stereotrode wire. The microdrive was lowered in 80- $\mu$ m steps between recording sessions until reaching a depth of  $\sim 2$  mm.

**Behavior.** Following  $\sim 5$  weeks of viral expression, mice were gradually food restricted to 85% of their body weight. Mice were then given 2 d of habituation to the T-maze, which consisted of 10–20 min of free exploration and foraging for food rewards while tethered to optical fibers and/or the recording tether. On the subsequent 2 d mice underwent behavioral shaping, which consisted of ten runs from the start box to a baited goal arm and back to the start box. Runs were forced choice in alternating directions and mice were habituated to laser illumination on half of the runs in a random interleaved fashion. Mice then commenced training on the DNMS T-maze for 6 consecutive days without laser illumination. Unlike the delayed alternation T-maze task, sample arm runs were pseudorandomly selected on a trial-by-trial basis. Within this window, all mice reached a criterion level of performance defined as 3 consecutive days above 70% correct. During the subsequent testing phase, in all experiments laser

illumination was delivered in a randomly interleaved fashion and with even distribution across trial types and animals. The experimenter was blind to the viral condition of mice during behavioral testing. For whole-trial light experiments, testing at 10-s and 60-s delays occurred on separate days. For physiology experiments comparing mPFC activity at 20-s and 60-s delays, testing was performed within the same session. For behavior-only and neurophysiology experiments, rewards consisted of either dustless pellets (Bio-Serv) or sweetened condensed milk ( $\sim 5$   $\mu$ L, 3:1 dilution), respectively. The intertrial interval for all experiments was fixed at 40 s. All behavior was conducted during the light cycle.

**Optogenetic parameters.** Pathway-specific optogenetic inhibition experiments were carried out using 10-mW, 532-nm constant light, delivered via flat-tipped, 200- $\mu$ m diameter, 0.22 NA fiber optics. In SSFO experiments, a 50-ms blue light pulse (473 nm, 4 mW) was used for opsin activation and a 50-ms yellow light pulse (593 nm, 4 mW) was used for opsin deactivation. Light output from fiber optics was predicted using a Monte Carlo modeling approach as previously published<sup>26</sup>. Absorption and scattering coefficients for 532-nm light were interpolated from data measured *in vivo*<sup>51</sup>. The predicted fluence rate was calculated according to our 10-mW output from 200- $\mu$ m, 0.22 NA fibers into a large cubic volume (6 mm<sup>3</sup>) of gray matter. The volume with a fluence rate above 7.5 mW/mm<sup>2</sup>, the approximate EPD50 of eArch3.0<sup>52</sup>, was calculated and plotted to scale on MD and mPFC brain slices from a mouse stereotactic reference atlas<sup>53</sup> to predict the effectively inhibited volume. Based on the model and on our viral expression pattern and fiber optic targeting, in all mice the mPFC projections to medial, central and lateral MD and the MD projections to dorsal and ventral mPFC were in part effectively inhibited. In our MD-to-mPFC task phase-specific experiments, our viral spread typically included expression in the paraventricular nucleus of the thalamus (PVT). However, viral spread in 5 of 33 mice was confirmed to spare the PVT. Our reported MD-to-mPFC delay-phase inhibition effect was clearly observable in four of the five mice (Light OFF, 75%  $\pm 2.1$ ; ON delay, 67%  $\pm 2.0$ ).

**Data acquisition.** Recordings were amplified, bandpass-filtered (1- to 1,000-Hz LFPs; 600- to 6,000-Hz spikes) and digitized using a Digital Lynx system (Neuralynx). LFPs were collected at 2 kHz, while spikes were detected by online thresholding, collected at 32 kHz and sorted offline. Single units were automatically clustered using Klustakwik (Ken Harris), based on spike-sorting of the first two principal components, peak voltage and energy from each stereotrode channel. Clusters were then accepted, merged or removed based on isolation distance, visual inspection of feature segregation, interspike-interval distribution, cross-correlation in spike timing for simultaneously recorded units and stability across recording session.

**Single-unit analysis.** In MD-to-mPFC experiments we isolated a total of 891 and 686 single units in 9 eArch and 9 eYFP animals, respectively. Of these, 538 eArch and 447 eYFP units were considered well-isolated, while the remainder of clusters were modestly contaminated with multiunit activity. To assess significantly light-modulated units, we considered only well-isolated clusters. We found that MD-to-mPFC inhibition significantly decreased (17%, 92 single units) and increased (15%, 83 single units) firing rates ( $P < 0.05$ , bootstrap followed by permutation test). This is consistent with monosynaptic inhibition and polysynaptic disinhibition of cortical projection neurons via fast-spiking interneurons, as has been described for prefrontal-projecting MD neurons in the mouse<sup>54</sup>. Results were similar when all clusters were included (136 of 891 units decreased firing rates, 134 of 891 increased firing rates in eArch; 52 of 686 units decreased firing rates and 56 of 686 units increased firing rates in eYFP). Significantly light-modulated mPFC single units were determined using bootstrapping. Specifically, light OFF and light ON spike-trains were randomly shuffled 30,000 times. If the observed light OFF/ON firing rate difference was greater than 95% of the firing rate difference from shuffled data, single units were deemed light-responsive. For all analyses of task-modulated single-unit activity, we included all 891 eArch and 686 eYFP units.

In vHPC-to-MD experiments, we isolated a total of 800 single units in 6 eArch-expressing mice. In this cohort of mice, we carried out within-session testing at 60-s delays with interleaved light-OFF, light-ON sample and light-ON delay trials, followed by light-OFF testing at 20-s delays. We found that 657/800 units were stable, well-isolated and retained cluster features across 60-s and 20-s testing and were therefore included for analysis in **Supplementary Figure 9**. All



800 units were used for analysis of task-modulated activity with and without vHPC-to-mPFC inhibition.

The preferred arm of each single unit was determined from the mean firing rate  $\pm$  500 ms around goal arrival on all left-visited versus right-visited trials in the sample or choice task phases. The observed preference during either sample or choice arm visits was then used for delay phase activity. *z*-scored firing rates for arm preference were then calculated in 100-ms (sample and choice phases) or 1-s (delay phase) bins, based on the mean bin  $\times$  bin firing rates across ITIs and the s.d. between bins. The average firing rate within  $\pm$ 500 ms of sample goal arrival on all left-versus-right trials was used to determine the significance of spatial tuning across all mPFC neurons (Wilcoxon's rank-sum test,  $P < 0.05$ ).

Delay-modulated activity was determined from *z*-scored firing rates calculated in 1-s bins based on the mean bin  $\times$  bin firing rate across ITIs and the s.d. between bins. If a single unit exhibited a *z*-scored firing rate beyond  $\pm 2$  s.d. for two or more consecutive bins, it was classified as a delay-elevated or delay-suppressed unit, respectively. The same criterion was used on shuffled versions of the entire MD-to-mPFC and vHPC-to-mPFC datasets. Shuffling was performed in a trial-by-trial manner that preserved the temporal structure of spikes. Specifically, each trial spike-train was treated as a continuous circular vector, and a randomly selected time point in each was designated as time 0. This was performed 1,000 times for each trial across all neurons.

The pairwise distance in firing rate across time in delay-elevated neurons was used for clustering into six groups using the 'kmeans' function in Matlab. The percentage of variance as a function of the number of clusters was used to estimate optimal cluster number. Six clusters were sufficient to explain ~50% of the variance and parceling the data into greater or fewer than six clusters neither improved visualization of groups nor altered the observed effects.

**Directionality analyses.** Functional directionality based on mPFC spikes and MD LFP was performed by successively calculating the pairwise phase comparison (PPC)<sup>55</sup> of mPFC spikes to MD LFP when shifting mPFC spikes in 10-ms steps  $\pm$  100 ms. MD LFP signal was first digitally bandpass-filtered (13–30 Hz) using a zero-phase-delay filter (filter0, provided by K. Harris and G. Buzsaki) and the Hilbert transform of the bandpass-filtered signal was calculated to obtain oscillatory phase. The magnitude of phase-nonuniformity of spike times relative to the filtered LFP oscillation was then calculated at each temporal offset during each task phase (sample, delay or choice). Only single units that exhibited Bonferroni-corrected PPC values at peak lag (Rayleigh's circular test,  $P < 0.0024$ ) were used for analysis. In order to avoid spuriously high or low PPC values, only units that fired at least 100 spikes per condition were used. We chose to bandpass-filter in the beta-frequency range given our previous results showing task modulation of MD–mPFC beta synchrony<sup>9</sup>. While we did not observe effects of task phase on directionality when filtering at low (40–70 Hz) or high (70–120 Hz) gamma bands, filtering at theta frequency (4–12 Hz) produced results similar to those reported here. Prior to commencing analysis, we excluded 344 single units due to improperly placed LFP electrodes or significant noise contamination in LFP signal during recording sessions.

Functional directionality based on MD and mPFC LFPs was performed as previously described<sup>27</sup>. Briefly, MD and mPFC LFP were bandpass-filtered as

described above. The instantaneous amplitude for all points in the MD and LFP signal was calculated and the cross-correlation between amplitudes of the two signals was computed using the Matlab function 'xcorr'. This was done over lags ranging from +100 to –100 ms in 1-ms shifts. We included 90 recording sessions in the analysis.

**Statistics.** A two-way repeated measures ANOVA was used to assess significant interactions of light and virus in all behavioral experiments. Throughout, where significant interactions emerged, *post hoc* two-tailed *t* tests were performed for paired comparisons between light OFF and light ON conditions, unless otherwise stated. When data was nonparametric, we used Wilcoxon's signed-rank and rank-sum tests for paired and unpaired observations, respectively. Sample sizes for all experiments were based on previous work<sup>10,18</sup> and are reported in all figure legends along with the *P* values for all statistical comparisons. Where appropriate, Bonferroni-corrected *P* values were used and indicated for multiple comparisons. For comparison of proportions we used two-sample Kolmogorov-Smirnov goodness-of-fit tests. For linear regression fit of 60-s/20-s peak firing times we used the Matlab function 'fitlm' to perform a robust regression using the bisquare weighting function.

**Histology.** At the end of experimentation, mice were transcardially perfused with PBS followed by 4% PFA. For neurophysiology experiments, electrolytic lesions were induced at each recording site by passing current (50  $\mu$ A, 20 s) through electrodes before perfusion. Fixed tissue was then sectioned (50  $\mu$ M) using a vibratome and mounted on slides with Vectashield mounting medium containing DAPI (Vector Labs). Direct fluorescence of eArch-eYFP or eYFP was then examined under an epifluorescent microscope (Zeiss) to assess the extent of viral spread and axon-terminal expression pattern. Locations of recording site lesions were confirmed with visualization under DAPI (**Supplementary Figs. 10 and 11**). Two mice were excluded from MD LFP analyses due to failed electrode targeting.

A **Supplementary Methods Checklist** is available.

**Data availability.** The data that support the findings of this study are available from the corresponding author upon reasonable request.

**Code availability.** Matlab code used for analysis of the data that support the findings of this study is available from the corresponding author upon reasonable request.

51. Johansson, J.D. Spectroscopic method for determination of the absorption coefficient in brain tissue. *J. Biomed. Opt.* **15**, 057005 (2010).
52. Mattis, J. *et al.* Principles for applying optogenetic tools derived from direct comparative analysis of microbial opsins. *Nat. Methods* **9**, 159–172 (2011).
53. Paxinos, G. & Franklin, K.B.J. *The Mouse Brain in Stereotaxic Coordinates*. (Academic Press, 2001).
54. Delevich, K., Tucciarone, J., Huang, Z.J. & Li, B. The mediodorsal thalamus drives feedforward inhibition in the anterior cingulate cortex via parvalbumin interneurons. *J. Neurosci.* **35**, 5743–5753 (2015).
55. Vinck, M., van Wingerden, M., Womelsdorf, T., Fries, P. & Pennartz, C.M. The pairwise phase consistency: a bias-free measure of rhythmic neuronal synchronization. *Neuroimage* **51**, 112–122 (2010).

---

## Erratum: Thalamic projections sustain prefrontal activity during working memory maintenance

Scott S Bolkan, Joseph M Stujenske, Sebastien Parnaudeau, Timothy J Spellman, Caroline Rauffenbart, Atheir I Abbas, Alexander Z Harris, Joshua A Gordon & Christoph Kellendonk

*Nat. Neurosci.*; doi:10.1038/nn.4568; corrected online 5 May 2017

In the version of this article initially published online, the rightmost coronal section was missing from the illustration in Figure 1d. The error has been corrected in the print, PDF and HTML versions of this article.

## Publisher Correction: Thalamic projections sustain prefrontal activity during working memory maintenance

Scott S Bolkan, Joseph M Stujenske, Sebastien Parnaudeau, Timothy J Spellman, Caroline Rauffenbart, Atheir I Abbas, Alexander Z Harris, Joshua A Gordon and Christoph Kellendonk

Correction to: *Nature Neuroscience* <https://doi.org/10.1038/nn.4568>, published online 3 May 2017.

In the version of this article initially published, the title of ref. 45 was given as “Sustaining cortical representations by a content-free thalamic amplifier.” The correct title is “Thalamic amplification of cortical connectivity sustains attentional control.” The error has been corrected in the HTML and PDF versions of the article.

Published online: 31 May 2018

<https://doi.org/10.1038/s41593-018-0132-2>